Supplementary materials

Following four ECAP deformations at RT, the commercial Al7075 exhibited an equiaxial grain distribution, as depicted in Figure S1. The average grain size was approximately 4.5 μm, with the <111> direction displaying significant anisotropy. This observation is consistent with the ideal pure shear deformation mechanism associated with ECAP. Post-deformation, the influence of dynamic recrystallization (DRX) altered the grain boundary orientation difference, increasing the frequency of high-angle grain boundaries (HAGB, >15°) to 41.8%, as shown in Figure S1(b). Nonetheless, low-angle grain boundaries (LAGB, 2°~15°) still constituted 58.2% of the total, indicating incomplete recrystallization of the fine-grained BM. Al7075 have high stacking fault energy (SFE), which facilitates dislocation cross-slip and climbing during plastic deformation, leading to continuous dynamic recrystallization (CDRX) and geometric dynamic recrystallization (GDRX) mechanisms [1, 2]. The grain orientation spread (GOS) in the fine-grained BM and its quantitative distribution are illustrated in Figure S1(c). The GOS values associated with recrystallized, sub-structured, and deformed grains range from 0°−2°, 2°−3° and 3°−15°, respectively, with a significant enhancement in sub-structured features corresponding to the substantial proportion of LAGBs. The most effective method for qualitative evaluation of lattice distortion is the GOS method, while the grain dislocation density can be assessed by analyzing the color depth [3]. The kernel average misorientation (KAM) diagram, shown in Figure S1(d), assesses the level of local deformation in the fine-grain BM, revealing an increase in local deformation correlated with a higher average geometrically necessary dislocation (GND) density. After four ECAP deformations, the distribution of GND becomes homogeneous, predominantly concentrated near the grain boundaries, with an elevated number of dislocations in the fine grain, consistent with the GOS diagram. The orientation distribution function (ODF) and polar diagram for the fine-grain BM are presented in Figure S2(e). The crystal plane texture orientation that exhibits the strongest response is the (111) plane, characterized by an Euler angle of 45°. The primary texture types observed in the fine-grained BM are Rotation Brass {111}<112> and γ-fiber {111}<110>, with sub-strong point texture types including Brass {110}<112> and S {123}<634>. This outcome aligns with the grain inverse pole figure (IPF) direction shown in Figure S2(a), demonstrating that ECAP effectively imposes a pure shear deformation mechanism.

The thermal cycling (TC) curve of the FSW joint weld is depicted in Figure S2, which illustrates the impact of various cooling conditions on the welding process. The data indicate that the implementation of FC significantly influences the thermal characteristics of the weld. Specifically, the peak temperature of the weld is reduced by 105 °C, a change highlighted by the arrow in the figure, while the cooling rate experiences a notable increase of 56.4%. The surface appearance of the welds also varies with the cooling conditions. The FC-FSW weld displays a smooth and flash-free surface, indicative of effective cooling and stable material flow during the welding process. In contrast, the RT-FSW weld shows more pronounced surface irregularities, particularly when subjected to high-temperature cycling (HTC). These irregularities include significant friction traces, suggesting that the higher temperatures encountered during RT-FSW may exacerbate surface degradation and deformation issues.

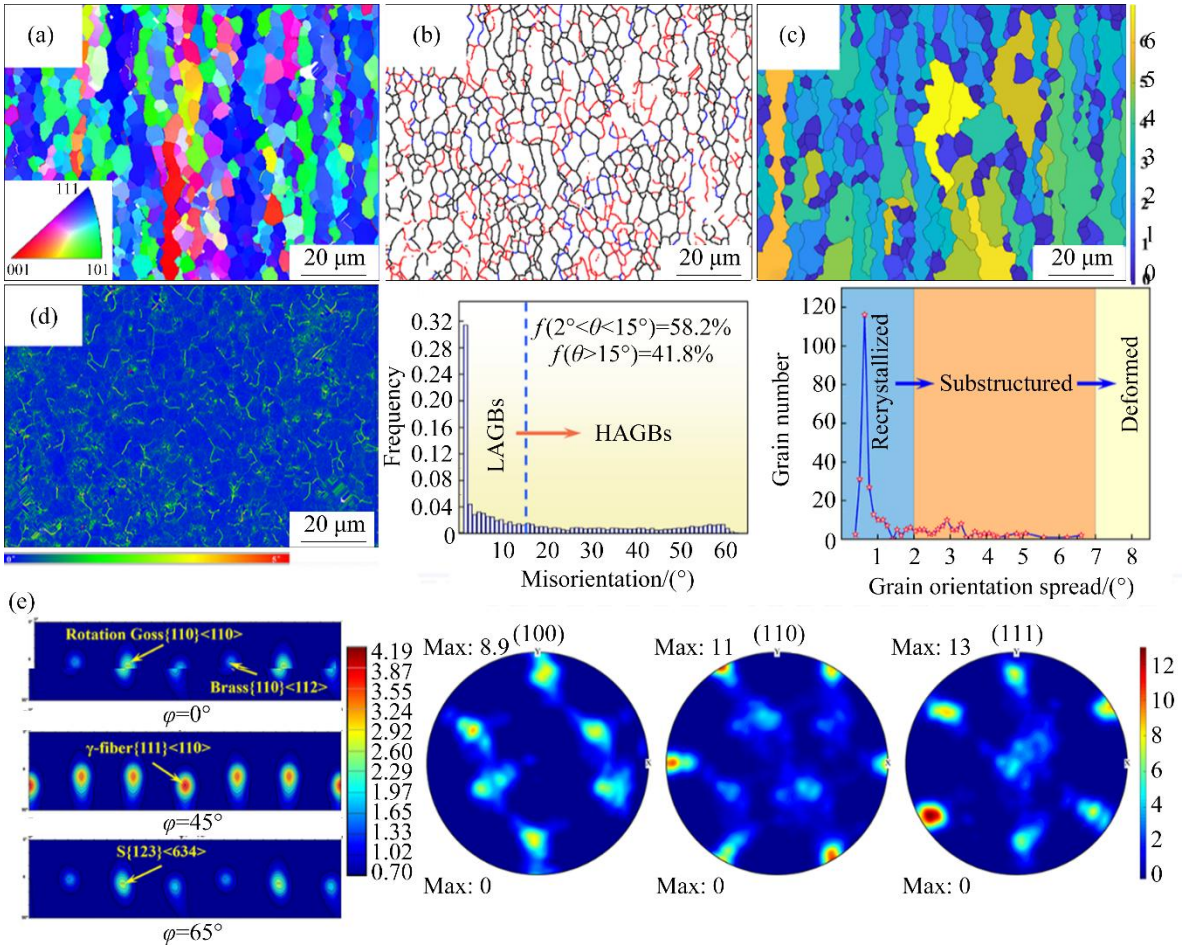

Figure S1 Microstructure of fine-grained BM: (a) Inverse pole figure; (b) Grain boundary distribution and proportion of their orientation difference; (c) Diagram of grain orientation spread; (d) Diagram of geometrically necessary dislocation (e) Orientation distribution function and polarity diagram

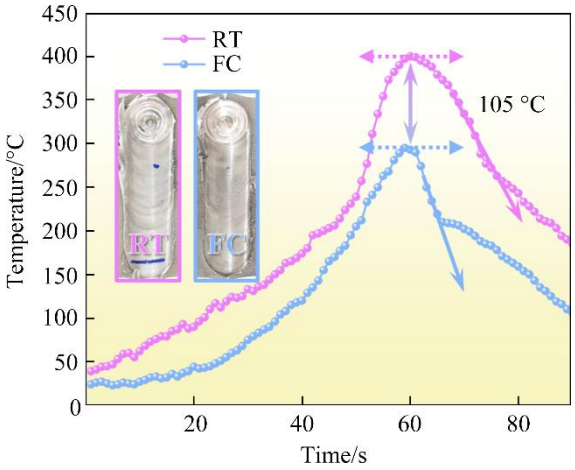

Figure S2 Macroscopic morphology and thermal cycling curves of joints

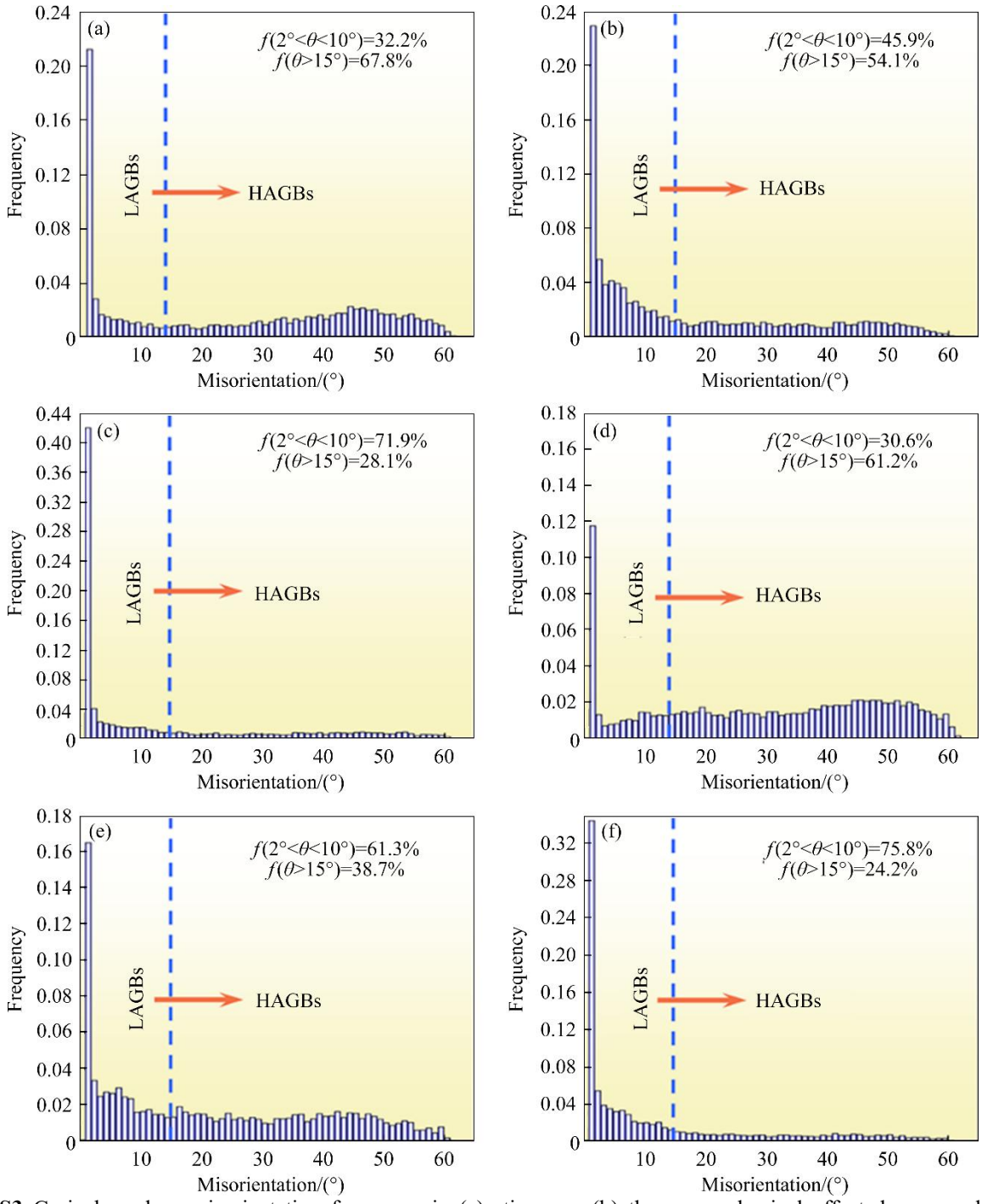

Figure S3 Grain boundary misorientation frequency in (a) stir zone, (b) thermo-mechanical affected zone and (c) heat-affected zone by forced-cooled friction stir welding, and in (d) stir zone, (e) thermo-mechanical affected zone and (f) heat-affected zone by room temperature friction stir welding

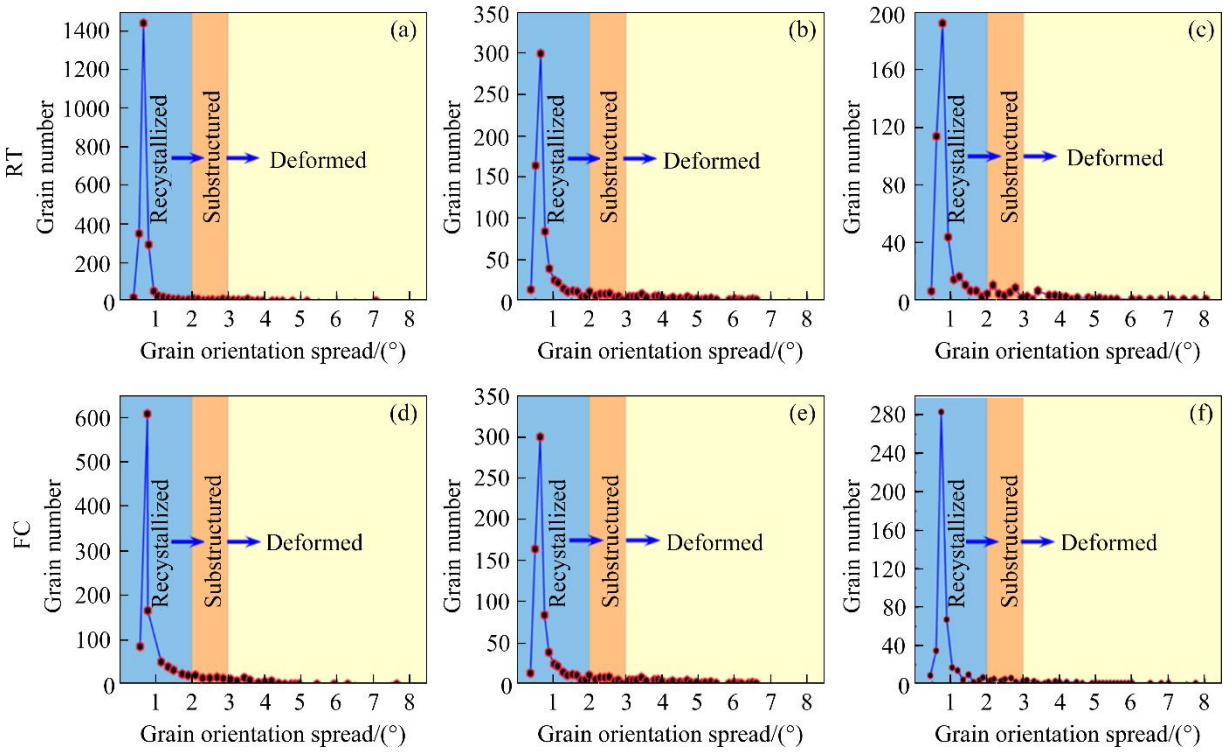

Figure S4 Number of grains with different GOS values in (a) stir zone, (b) thermo-mechanical affected zone and (c) heat-affected zone by forced-cooled friction stir welding, and in (d) stir zone, (e) thermo-mechanical affected zone and (f) heat-affected zone by room temperature friction stir welding

Figure S5 provides a detailed analysis of the dislocation configurations and the types of precipitation phases in the fine-grained BM, illustrating how ECAP deformation at RT crucially influences the dislocation density within the material. The matrix hosts a variety of finely dispersed precipitation phases, predominantly characterized by circular, elliptical, and rod-like shapes. Figure S5(a) specifically highlights the interactions between the precipitation phases and dislocation lines (illustrated with yellow and green circles), showcasing the complex nature of the underlying strengthening mechanisms. Currently, the principal mechanisms of interaction between dislocations and precipitation phases include dislocation cut-off and dislocation bypass. It is noteworthy that the strengthening effect of the dislocation cut-off is superior to that of the dislocation bypass mechanism. This distinction is critical, as it suggests that the dislocation cut-off contributes more effectively to the overall strength of the material, enhancing its structural integrity and performance in applications. These interactions are fundamental to understanding the mechanical properties and the enhancement of durability in alloy systems.

The analysis indicated that the predominant precipitation phases are Al_2Cu, $MgZn_2$, and Al_2CuMg (Figure S5(b)). HRTEM was employed to determine the lattice spacing of these precipitation phases. The crystal plane spacing of circular precipitation phases was measured using techniques such as Inverse Fast Fourier Transform (IFFT) and Fast Fourier Transform (FFT), with additional FFT diffraction calibration performed to ensure accuracy (as illustrated in Figure S5(c)). The predominant phase, identified as Al2Cu, exhibited minimal atomic misfit with the matrix, showing excellent interface structure matching and a coherent state, which effectively minimizes the elastic misfit energy between the Al_2Cu phase and the matrix (highlighted by yellow arrows). The elliptical precipitation phase, depicted in Figure S5(d), was identified as Al_2CuMg through FFT diffraction calibration and measurement of crystal plane spacing. Analysis of the atomic mismatch between the Al_2CuMg phase and the matrix boundary, along with the extent of distortion in the Al lattice structure of the matrix, indicates that this phase maintains a semi-coherent relationship with the matrix. The presence of edge dislocations near the Al_2CuMg phase helps to alleviate the lattice mismatch and minimizes the elastic strain energy at the interface, facilitated by interface misfit dislocation mechanisms. The rod-shaped precipitation phase shown in Figure S5(e) was identified as $MgZn_2$ through the application

of FFT diffraction calibration and IFFT for measuring crystal plane spacing. Observations of lattice fringes and atomic mismatches at the boundary between the $MgZn_2$ phase and the Al matrix suggest that this phase is incoherent with the matrix, with a significantly large lattice mismatch. This phase does not feature interface misfit dislocations due to the superimposition of the original lattices at the incoherent interface, leading to increased interface energy. The phase boundary transitions from coherent to incoherent, with a corresponding increase in interface energy. For coherent and semi-coherent phases, the low interface energy with the matrix facilitates the action of dislocations through a cutting mechanism. Conversely, the interface of the incoherent phase, characterized by high energy and resistance to deformation, compels dislocations to bypass the phase. This distinction in interface behavior significantly influences the mechanical properties and deformation mechanisms within the material.

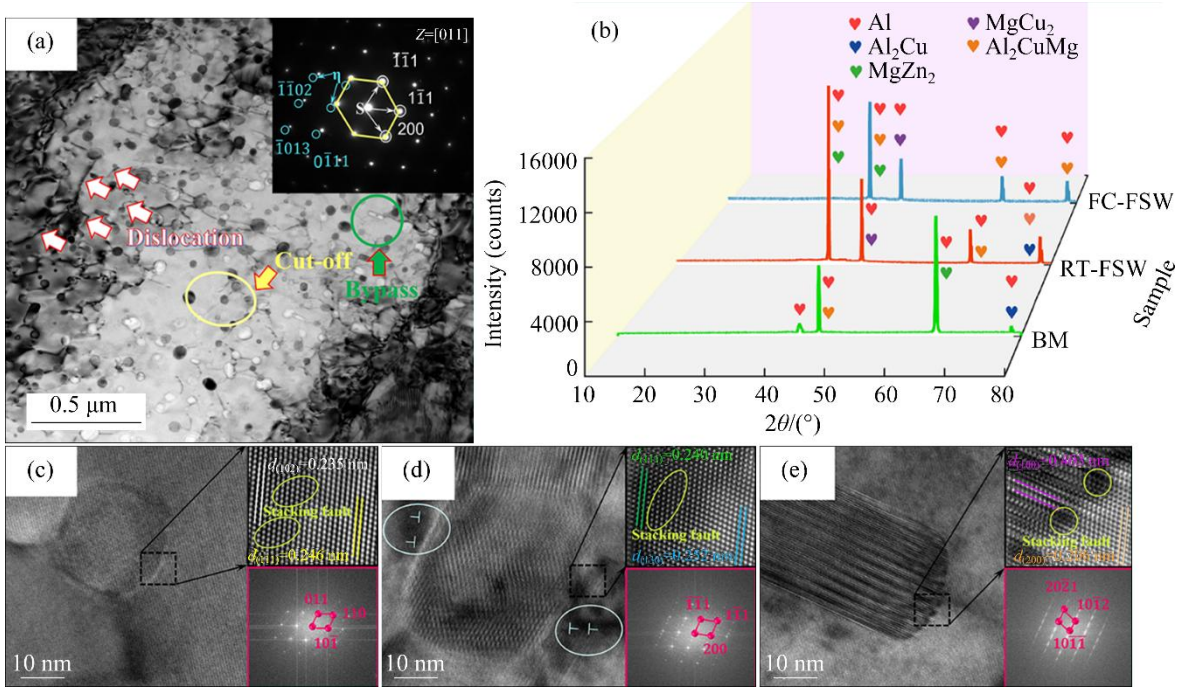

Figure S5 HRTEM microstructure and XRD phase of fine-grained BM: (a) Precipitation phase distribution; (b) XRD patterns; (c) Circular precipitation phase; (d) Elliptical precipitation phase; (e) Rod-like precipitation phase

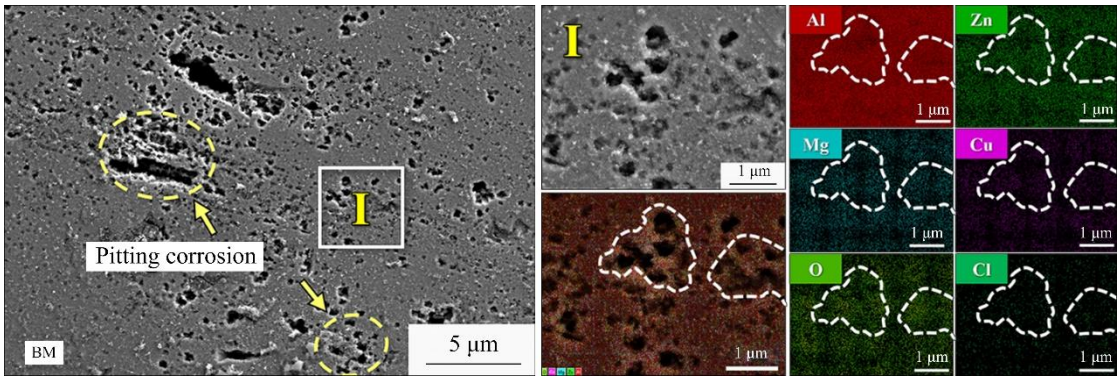

Figure S6 Corrosion morphology of fine-grained BM

References

[1] LUO Lei, YANG Bo-hai, YANG Xi-rong, et al. Effect of room temperature multi-pass ECAP deformation on mechanical properties and precipitation phase distribution of 7075 aluminium alloy [J]. Journal of Central South University, 2023, 30(2): 374−386. DOI: 10.1007/s11771-023-5267-y.

[2] ZHAO Shi-lin, ZHANG Hai-ming, CUI Zhen-shan, et al. Particle dispersion and grain refinement of in situ TiB_2 particle reinforced 7075 Al composite processed by elliptical cross-section torsion extrusion [J]. Journal of Alloys and Compounds, 2020, 834: 155136.

DOI: 10.1016/j.jallcom.2020.155136.

[3] MUKHOPADHYAY A, SAHA P, SINGH P K, et al. Development and analysis of a powder bed friction stir (PBFS) additive manufacturing process for aluminum alloys: A study on friction-stirring pitch (ω/v) and print location [J]. Additive Manufacturing, 2023, 72: 103618. DOI: 10.1016/j.addma.2023.103618.